Shang, Bin; Xu, Miao; Zhi, Zelun; Xi, Yuewei; Wang, Yanbing; Peng, Bo; Li, Peng; Deng, Ziwei

Synthesis of sandwich-structured silver@polydopamine@silver shells with enhanced antibacterial activities

Published in:
Journal of Colloid and Interface Science

DOI:
10.1016/j.jcis.2019.09.091

Published: 15/12/2019

Document Version
Peer-reviewed accepted author manuscript, also known as Final accepted manuscript or Post-print

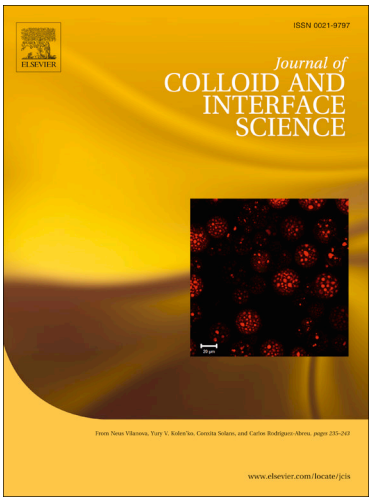

Synthesis of sandwich-structured silver@polydopamine@silver shells with enhanced antibacterial activities

Bin Shang, Miao Xu, Zelun Zhi, Yuewei Xi, Yanbing Wang, Bo Peng, Peng Li, Ziwei Deng

PII: S0021-9797(19)31134-8
DOI: https://doi.org/10.1016/j.jcis.2019.09.091
Reference: YJCIS 25461

To appear in: *Journal of Colloid and Interface Science*

Received Date: 29 August 2019
Revised Date: 24 September 2019
Accepted Date: 24 September 2019

Please cite this article as: B. Shang, M. Xu, Z. Zhi, Y. Xi, Y. Wang, B. Peng, P. Li, Z. Deng, Synthesis of sandwich-structured silver@polydopamine@silver shells with enhanced antibacterial activities, *Journal of Colloid and Interface Science* (2019), doi: https://doi.org/10.1016/j.jcis.2019.09.091

Synthesis of sandwich-structured silver@polydopamine@silver shells with enhanced antibacterial activities

Bin Shang [a†], Miao Xu [b†], Zelun Zhi [c], Yuewei Xi [d], Yanbing Wang [a], Bo Peng [e*], Peng Li [b,c*], Ziwei Deng [a*]

[a] Key Laboratory of Applied Surface and Colloid Chemistry, Ministry of Education, Shaanxi Key Laboratory for Advanced Energy Devices, Shaanxi Engineering Lab for Advanced Energy Technology, School of Materials Science and Engineering, Shaanxi Normal University, Xi'an, 710119, China.

[b] Key Laboratory of Flexible Electronics (KLOFE) and Institute of Advanced Materials (IAM) Jiangsu National Synergetic Innovation Center for Advanced Materials (SICAM)，Nanjing Tech University, Nanjing, 211816, China.

[c] Shaanxi Institute of Flexible Electronics (SIFE) & Xi'an Institute of Biomedical Materials Engineering (IBME), Northwestern Polytechnical University (NPU), 127 West Youyi Road, Xi'an 710072, China.

[d] Frontier Institute of Science and Technology, Xi'an Jiaotong University, Xi'an, 710054, China.

[e] Department of Applied Physics, Aalto University, Espoo FI-00076, Finland.

[†] These two authors contributed equally to this work.

Corresponding authors:

* Dr. Bo Peng, E-mail: pengbo006@gmail.com

* Prof. Peng Li, E-mail: iampli@nwpu.edu.cn

* Prof. Ziwei Deng, E-mail: zwdeng@snnu.edu.cn

ABSTRACT

The unique antibacterial characteristics of Ag nanomaterials offer a wide potential range of applications, but achieving rapid and durable antibacterial efficacy is challenging. This is because the speed and durability of the antibacterial function make conflicting demands on the structural design: the former requires the direct exposure of Ag to the surrounding environment, whereas the durability requires Ag to be protected from the environment. To overcome this incompatibility, we synthesize sandwich-structured polydopamine shells decorated both internally and externally with Ag nanoparticles, which exhibit prompt and lasting bioactivity in applications. These shells are biocompatible and can be used *in vivo* to counter bacterial infection caused by methicillin-resistant *Staphylococcus aureus* superbugs and to inhibit biofilm formation. This work represents a new paradigm for the design of composite materials with enhanced antibacterial properties.

Keywords: Sandwich structure; Nanocomposite shells; Ag nanoparticles; Polydopamine; Antibacterial activity.

1. Introduction

Silver has been utilized against bacterial contamination of water and food thousands of years ago [1,2]. It was later applied extensively as an antibacterial agent to prevent wound infection until the identification and the commercialization of the antibiotics. The selectivity and the effectiveness of the antibiotics led to a surge in their use in medicine, while the use of Ag materials declined. However, bacteria cannot develop resistance to Ag as they can to antibiotics, and widespread antibiotic resistance now provides impetus for the development of new antibacterial Ag materials [3–7].

Recent synthetic advances in nanotechnology have introduced Ag nanoparticles as a new form of Ag materials with unique bactericidal characteristics [6–8]. Thanks to their small size and high active surface, Ag nanoparticles exhibit superior bactericidal capabilities than their bulk forms [7–9]. The antibacterial activities of Ag nanoparticles are closely associated with their release of Ag ions, which are bioactive and interfere with vital enzymes in bacteria [7,8,10,11]. As such, the preparation of Ag nanomaterials that can achieve a prompt yet durable release of Ag ions at a high concentration could provide an potent solution to the challenge of effective inhibition of bacterial population growth [7]. Nevertheless, the design of such materials is challenging because the prompt ion-release and the durability of the function make contradictory demands on the structure of the nanomaterials. Rapid release requires the direct contact between Ag and the surrounding medium [12], while the durable release requires that the Ag nanoparticles are protected from the environment [13].

To satisfy these contradictory demands, we propose a unique concept for the design of Ag nanocomposite materials with enhanced antibacterial activity. We synthesize hollow polydopamine (PDA) colloidal particles that are internally and externally decorated with Ag nanoparticles via the sequential surface modification and the sacrificial template approaches,

giving rise to sandwich-structured Ag@PDA@Ag shells. These composite shells integrate the advantageous antibacterial features of the core@Ag and Ag@shell structured particles, enabling a prompt, intense, and durable release of Ag ions. Consequently, they exhibit superior antibacterial activity in inhibiting the growth of both Gram-negative bacteria, *Escherichia coli* (*E. coli*) and Gram-positive bacteria, *Staphylococcus aureus* (*S. aureus*). Additionally, these Ag@PDA@Ag shells are biocompatible and can be applied to treat *in vivo* methicillin-resistant *S. aureus* (MRSA) superbug infection and to inhibit biofilm formation. Hence these sandwich-structured shells represent a promising avenue towards advanced nanocomposites with enhanced bioactivity.

2. Experimental section

2.1. Materials

All chemicals are analytic grade and used as received, unless otherwise mentioned. Polyvinylpyrrolidone (PVP, molecular weight = 40000 g/mol), 3-hydroxytyramine hydrochloride (dopamine hydrochloride), and tris(hydroxymethyl) aminomethane (Tris-base, ≥ 99.8%) were purchased from Sigma-Aldrich. 2, 2'-azobisisobutyronitrile (AIBN) was acquired from Shanghai Chemical Reagent Co., Ltd., and was recrystallized in ethanol prior to use. Styrene (St) was bought from Tianjing Tianli Chemical Reagent Co., Ltd. and was distilled in vacuum to remove the inhibitor and subsequently stored at 4 ^{o}C until use. Ethanol, ammonia solution (28 wt% in water), silver nitrate (≥ 99.8%), hydrochloric acid (36 wt% in water), trichloromethane, nitric acid (65.0-68.0%), and sulfuric acid (98%) were supplied by Sinopharm Chemical Reagent Co. Ltd. Ultrapure water (>17 MΩcm^{-1}) used throughout the experiments was from a GZY-P10 water system.

2.2. Preparation of sandwich-structured Ag@PDA@Ag shells.

The synthesis involved the layer-by-layer decoration of monodisperse sulfated polystyrene (SPS) colloidal particles with Ag nanoparticles, a PDA shell and Ag nanoparticles in sequence, followed by the removal of the SPS cores. First, monodisperse polystyrene (PS) colloidal spheres were synthesized through dispersion polymerization and then sulfonated by sulfuric acid (98%), giving rise to uniform SPS colloids. The SPS particles were first separated by centrifugation, then cleaned with ultrapure water, and finally stored in water [14].

Second, the SPS particles were coated with Ag nanoparticles by *in situ* reducing $[Ag(NH_3)_2]^+$ ions using PVP. PVP plays two roles in the reaction, the first is as the reductant [15,16], and the other as the stabilizer [17,18]. Typically, a freshly prepared $[Ag(NH_3)_2]^+$ aqueous solution (1 mL, 0.29-1.17 M) was added to a mixture of SPS particles (0.3 g), ethanol (19.0 g) and PVP (0.05 g) at room temperature. After 2 h of stirring, the mixture was heated to 70 ^oC and the temperature was maintained for 7 h prior to cooling naturally [19]. The core-shell structured SPS@Ag nanocomposites were collected by centrifugation and rinsed with water and ethanol several times prior to drying in a vacuum.

Third, the SPS@Ag particles were coated with a PDA shell by mixing SPS@Ag particles (0.2 g) with a dopamine solution comprising dopamine (0.2 g) and Tris–HCl buffer (100 mL, 10 mM and pH 8.5) via sonication [20]. The mixture was magnetically stirred for 24 h prior to centrifugation, then rinsed with deionized water and finally dried in vacuum. The SPS@Ag@PDA particles were stored in air.

Finally, the SPS@Ag@PDA particles were decorated with Ag nanoparticles via an electroless Ag metallization [12,21,22]. Typically, the SPS@Ag@PDA particles (0.1 g) were dispersed into 50 mL of freshly prepared $[Ag(NH_3)_2]^+$ ion aqueous solution (0.012-0.048 M) by sonication. The $[Ag(NH_3)_2]^+$ ions were anchored by the active catechol and amine groups presented in PDA, and

simultaneously *in situ* reduced to metallic Ag nanoparticles [23,24], resulting in SPS@Ag@PDA@Ag particles. Actually, the reduction of Ag ions into metallic Ag nanoparticles is mainly ascribed to the abundant catechol groups presented in polydopamine. These catechol groups can release electrons when they are oxidized into their corresponding quinone derivatives, which enable to trigger the reduction of noble metal ions into metallic nanoparticles [25,26]. The SPS cores were then removed with trichloromethane. The sandwich-structured Ag@PDA@Ag shells were collected by centrifugation and stored in a glass vial for further use.

For comparison, a series of shells including PDA, Ag@PDA, and PDA@Ag particles were also synthesized following a similar strategy. Their formulations are detailed in Table S2.

2.3. Hemolysis Assay

The hemolysis assay was carried out according to an existing protocol [27]. In detail, the fresh rat erythrocyte cells were collected from the Sprague-Dawley immune-competent rats (age: 7-9 weeks, Harlan, Horst, the Netherlands), and the protocol was approved by the Animal Ethical, Care and Use Committee at Xi'an Jiaotong University, China. Erythrocyte cells were first suspended in Tris-buffer, then centrifuged (500 *g* for 10 min) and rinsed with Tris-buffer three times, and finally diluted to a concentration of 5.0 % (v/v) with Tris-buffer. The Ag@PDA@Ag shell suspension was transferred into a 96-well microplate (80 μL for each well) at different concentrations. An equivalent volume of erythrocyte suspension was then added to each well. Positive and negative controls were performed using 0.1% Triton X-100 in Tris-buffer and Tris-buffer without shells, respectively. The microplate was first incubated at 37 ^{o}C for 1 h with a gentle shaking (150 rpm), and then centrifuged at 1000 *g* for 10 min. The supernatant (100 μL) from each well was then pipetted into the wells of a new microplate. A further 100 μL of Tris-buffer was added to each well to fix the final volume at 200 μL. The absorbance at 540 nm was determined

by using a microplate spectrophotometer (BIO-RAD Benchmark Plus, U.S.A.). The percentage of the hemolysis was calculated based on the following equation:

$$\text{Hemolysis (\%)} = [(A_{sample} - A_{Tris\text{-}buffer}) / (A_{Triton\ X} - A_{sample})] \times 100\% \quad (1)$$

where A_{sample}, $A_{Tris\text{-}buffer}$ and $A_{Triton\ X}$ are the absorbance of Ag@PDA@Ag shells, and negative and positive controls, respectively.

2.4. In vitro cytotoxicity and cell viability evaluation

C2C12 cells (the clonal myoblastic cell line, bought from ATCC) were grown in Dulbecco's Modified Eagle Medium (DMEM, Invitrogen) with 10% (v/v) fetal bovine serum (FBS), 100 U/mL penicillin and 100 μg/mL streptomycin, and incubated in a humidified atmosphere containing 5% CO_2 at 37 °C. The C2C12 cells were then seeded in 96-well plates at a density of around 8000 cells per well.

The *in vitro* cytotoxicity of the Ag@PDA@Ag shells for C2C12 cells was tested using an Alamar blue assay. Specifically, C2C12 cells were incubated in a standard culture medium in the presence of the Ag@PDA@Ag shells at various concentrations (10, 20, 40, 60, 80, and 100 μg/mL) for 24 h. Meanwhile, the control groups containing culture medium alone were also prepared. Subsequently, 10 μL of Alamar blue was added to each well, and the plates were incubated for 4 h at 37 °C. The absorbance of each well was measured with a microplate reader (SpectraMax i3, Molecular Devices, U.S.A.) at 530 and 600 nm, respectively. The cell viability ratio was determined by comparing the absorbance of the wells with those of the control wells containing cell culture medium only.

2.5. Antibacterial assays

To evaluate the antibacterial activity of the shells, two bacterial species, *Escherichia coli*

(ATCC 25922, Gram-negative) and *Staphylococcus aureus* (ATCC 29213, Gram-positive) were selected as the bacterial models. Bacteria cells were incubated overnight in an MHB (Mueller-Hinton Broth) medium at 37 ^{o}C in an Orbital Shaker with a speed of 200 rpm, and subsequently collected at the exponential growth phase by centrifugation at 5000 rpm for 5 min. The bacterial cells were washed three times with the phosphate buffer saline (PBS), and then re-suspended in the PBS at concentrations ranging from 10^6 to 10^7 colony-forming units (CFU) per milliliter. Later, 50 μL of bacterial suspension were added to 5 mL of MHB with shells. The suspensions were cultured at 37 ^{o}C, and bacterial survival was detected with an ultraviolet spectrophotometer at a wavelength of 600 nm. The O.D. (optical density) of the mixture was checked hourly from 0 to 20 h.

To further examine the antibacterial activities of the shells, the bacteria were stained by using the live/dead backlight bacterial viability kits, following a standard protocol (Invitrogen) [28]. Briefly, 10 μL of a fluorescent dye was added to 10 μL of bacterial suspension. The samples were then mixed intensively and incubated at room temperature in the dark for 30 min. The cells were imaged with an inverted fluorescence microscope (IX53, Olympus, Japan).

2.6. In vivo wound infection assay

The *in vivo* animal experiments [29] were approved by the Institutional Animal Care and Use Committee at Nanjing Tech University. The pathogen-free Sprague−Dawley immune-competent male rats (Harlan, Horst, the Netherlands), 7-9 weeks old (200−220 g in weight), were obtained from Nanjing Medical University. The rats were individually raised in cages at a standardized temperature for 2 days. The rats were anaesthetized with 10% chloral hydrate (30 mg/kg), and two partial thickness wounds were made on the right and the left sides of the backbone with a surgical scalpel covering a rectangular surface (length of about 10 mm, see SF-12). 10 μL aliquot of MRSA

bacterial solution (10^8 CFU) was applied topically to the wounds. After 10 min, 10 μL of Ag@PDA@Ag (100 μg/mL) PBS dispersion was added to the right wound and the same volume of PBS to the left wound. After 4 days, skin tissue samples from the wound sites were collected for histological staining and biochemical analysis.

2.7. Histological examination

For histological examination, the skin wound specimens were fixed in 10% buffered formalin and embedded in paraffin, and sections (3 μm thick) were stained with hematoxylin and eosin (HE) staining. The histological observations were made with an optical microscope.

2.8. Bacterial load evaluation in skin

The bacterial load in the skin was determined following a reported method [30]. Briefly, the skin (0.2 g) was removed aseptically from the rats and homogenized in 2 mL of PBS (0.1 M, 7.2 pH). The tissue homogenates were serially diluted. The bacterial load was determined by plating the dilution on nutrient agar plates and was enumerated in terms of CFU/mL.

2.9. Characterization

The surface morphologies of the samples were characterized by transmission electron microscopy (TEM, JEOL JEM-2100, Japan). All samples were dispersed in ethanol and dried onto carbon-coated copper grids prior to observation. The mean diameters of the particles were calculated as the average of the measured diameter of over 100 particles from TEM images, and the polydispersity of the samples was calculated based on the standard deviation:

$$Polydispersity = Standard\ deviation/mean\ diameter \quad (2)$$

Elemental mapping was performed by energy-dispersive X-ray spectroscopy attached to the TEM. Scanning electron microscopy (SEM, Hitachi SU8020, Japan) was used to characterize the surface

morphologies of the particles and the bacterial cells. Particles were dispersed in ethanol and were dried on silicon wafers at room temperature before observation. The cells were treated based on a reported protocol [2,31] and were observed with a field emission scanning electron microscope (FESEM, Quant 250, FEI, U.S.A.). Thermogravimetric analysis (TGA) was performed on an SDT Q600 (TA Instruments. U.S.A.). Sample powder was heated from 30 to 800 ^{o}C at a rate of 10 ^{o}C/min^{-1} under a nitrogen atmosphere with a flow rate of 50 mL/min^{-1}. Powder X-ray diffraction (XRD) was performed on a DX-2700 X-ray diffractometer equipped with a Cu tube and a diffracted beam curved graphite monochromator operating at 40 kV and 30 mA. The crystal structure identification was carried out by scanning the sample powders supported on a glass substrate with a scanning rate of 0.02 degrees (2θ) per second ranging from 10 to 90° (2θ). X-ray photoelectron spectroscopy (XPS) measurement was carried out on an AXIS Ultra X-ray photoelectron spectrometer (Kratos Analytical Ltd., the U.K.) equipped with a monochromatized Al K X-ray source (1486.6 eV). All binding energies were calibrated using the containment carbon (C1s = 284.6 eV). An inductively coupled plasma mass spectrometer (ICP-MS, M90) was used to measure the Ag ion release from shells. 5 mg of the sample were dispersed into ultrapure water (20 mL), and then shaken in an orbital shaker with a speed of 100 rpm for periods ranging from 1 to 120 h. At selected intervals, the sample solution was centrifuged, and 1 mL of the supernatant was transferred to a diluted nitric acid solution (9 mL, 1 v/v %). The Ag ions in the diluted supernatant were measured with ICP-MS.

3. Results and discussion

The synthesis of sandwich-structured Ag@PDA@Ag shells is schematically described in Fig. 1a. It consists of four major steps and integrates a sacrificial template, metallization of Ag ions,

and PDA chemistry. These steps are conducted in succession: 1) monodispersed sulfonated polystyrene (SPS) particles (see Fig. 1b and Table S1 in the Supplementary Information, SI) are decorated with Ag nanoparticles that are reduced by polyvinylpyrrolidone [15,32], resulting in SPS@Ag core-shell particles; 2) SPS@Ag particles are coated with PDA shells (57 nm in thickness, see Table S1 in the SI) by polymerizing dopamine in a weakly alkaline environment [20,26,33], yielding SPS@Ag@PDA core-shells; 3) PDA shells enable the *in situ* reduction of $[Ag(NH_3)_2]^+$ ions into Ag nanoparticles [21,25,26], allowing the formation of SPS@Ag@PDA@Ag core-shells; 4) sandwich-structured Ag@PDA@Ag shells (1526 nm in diameter, see Table S1) are obtained after the removal of the SPS cores with $CHCl_3$. Note that the removal of the polystyrene cores are necessary concerns three aspects: 1) Polystyrene is not bio-compatible, [34,35] the removal of which would improve the bio-compatibility of the samples; 2) the removal of the polystyrene core can directly increase the weight fraction of bioactive Ag nanoparticles within the samples, enhancing the antibacterial performance of the samples; 3) the dissolution of the polystyrene core leads to a void in the particles, which facilitates the further internal functionalization of the particles or the storage of the guest molecules [36,37]. The structures of the products from each step characterized with transmission electron microscopy (TEM) are shown in Fig. 1b-f (also see Fig. S1-4a in SI). X-ray photoelectron spectroscopy is used to determine the surface compositions of the products, as displayed in Fig. 1g (also see Fig. S1c, S2d, S3d, and S4c). These are consistent with X-ray diffraction results (Fig. S1d, S2c, and S4d). In the end, the sandwich structures of the Ag@PDA@Ag shells are confirmed by elementally mapping the shells as shown in Fig. 1h (also see Fig. S5).

Next, we demonstrate that the morphology of the interior and exterior Ag shells can be tuned independently by altering the amount of Ag precursors fed during steps 1 and 4, respectively.

Similarly, the mean sizes of both the inner and outer Ag nanoparticles decrease with an increase in the amount of Ag precursors, which is in line with previous results [12,15]. The inner Ag nanoparticles are smaller than the outer ones (see Fig. 2, S6a, and S7). This may be ascribed to the diverse synthetic protocols applied during steps 1 and 4. In step 1, polyvinylpyrrolidone serves as both a reductant [32] and a stabilizer [15] for the smaller Ag nanoparticles. In contrast, in step 4, Ag precursors are *in situ* reduced into nanoparticles by PDA shells, and grow into larger nanoparticles because of insufficient stabilization (Fig. S6) [12]. In addition, increasing the amount of Ag precursors leads to a rise in the load of the Ag nanoparticles (Fig. S6b and S7). The synthetic ingredients and the sizes of the samples are summarized in Table S2.

The antibacterial activity of Ag nanocomposites relies on their structures [8]. First, we evaluate the antibacterial activity of Ag@PDA@Ag shells against Gram-negative *Escherichia coli* (ATCC25922) bacteria and Gram-positive *Staphylococcus aureus* (ATCC29213), in comparison with those of PDA, Ag@PDA, and PDA@Ag shells, by culturing the mixtures of the shells and bacteria on Lysogeny broth-agar plates. After 12 h incubation, Ag@PDA@Ag shells exhibit the highest antibacterial activity, followed by Ag@PDA, and finally PDA@Ag shells. PDA shells do not indicate obvious bioactivity as demonstrated in Fig. 3a and b. Next, we quantify and compare the antibacterial performance of different shells by monitoring bacterial growth over time in the presence of shells at concentrations of 100 μg/mL in Mueller-Hinton broths for up to 20 h. Ag@PDA@Ag shells suppress the bacterial growth of both *E. coli* and *S. aureus* for longest (~18 h), followed by Ag@PDA (~13 h) and finally PDA@Ag (~7 h) as indicated in Fig. 3c and d.

The antibacterial activity of Ag materials primarily depends on the release of Ag^+ ions, although the precise mechanism is still under debate [7,8,11,38]. The concentrations of Ag^+ ions released from shells are monitored with an inductively coupled plasma mass spectrometer [39]. We observe

that PDA@Ag shells release Ag^+ ions faster but to a lower plateau concentration than Ag@PDA shells do (Fig. 3e), although the former contain more Ag than the latter (Fig. S8). This may be caused by the difference in size between the inner and outer Ag nanoparticles (see Fig. 2 and Table S2) [40]. Interestingly, Ag@PDA@Ag shells integrate the advantageous features of PDA@Ag and Ag@PDA shells, resulting in a more rapid, intense, and durable release of Ag^+ ions (Fig. 3e). This is in accordance with the Ag^+ release rate analyses in Fig. 3f, where Ag@PDA@Ag shells demonstrate a higher Ag^+ release rate than the other two types of shells. These results also reflect the relative antibacterial performance of various shell-types (Fig. 3c and d). The augmented, yet nondurable Ag^+ release from PDA@Ag shells leads to a short inhibition period, whereas Ag@PDA shells liberate Ag^+ ions more slowly but longer resulting in prolonged antibacterial activity. The sandwich-structured Ag@PDA@Ag shells combine the structural advantages of Ag@PDA and PDA@Ag shells, thus exhibiting both high antibacterial activity and long-term efficacy.

Since Ag is the key bioactive component in shells, we next aim to tune the antibacterial results by controlling the concentration of Ag. To achieve this goal, two approaches are feasible: these are either adjusting the Ag content within the shells or adjusting the concentration of Ag@PDA@Ag shells. As displayed in Fig. S9, an increase in the concentrations of Ag nanoparticles and Ag@PDA@Ag shells prolongs the inhibition of the bacterial growth for both *E. coli* and *S. aureus*. The cell membranes of the bacteria are damaged and the bacteria collapse after the addition of the shells, eventually leading to bacterial death (Fig. S10). This agrees with previous results, where Ag materials have been shown to deactivate micro-organismal cells by interacting with sulfide-groups within enzymes and proteins, and causing structural changes and functional damage to the cell membrane, leading to cell death [7,38,40].

Prior to testing the *in vivo* application of Ag@PDA@Ag shells, we evaluate their biocompatibility as shown in Fig. 4. First, a hemolysis assay of the shells is conducted by incubating them with the rat erythrocyte cells. As the shell concentrations increase up to 1250 μg/mL, a minor hemolysis effect (< 8%) is observed as indicated in Fig. 4a. Then, the cytotoxicity of the shells is estimated with C2C12 cells using an alamar blue assay. Cell viability remains high (~80%) even as the concentration of the shells increases to 100 μg/mL, hinting that the shells are benign and biocompatible.

Finally, we demonstrate the *in vivo* antibacterial utilization of Ag@PDA@Ag shells in wound-healing in rats. Wounds on the backs of the rats are made by incising the skin (Fig. 5a and Fig. S11) and are then infected with MRSA superbugs, without a treatment with shells in the control batch (Fig. 5a-1) [29]. In the treated batch, Ag@PDA@Ag-iii shells are added to the infected wounds to counter the bacterial infection (Fig. 5b-1). After 4 days, while the treated wounds heal (Fig. 5b-2) well with a low load of viable bacteria (inset in Fig. 5b-2 and Fig. S12), the control wounds do not heal (Fig. 5a-2), and exhibit a high bacterial content (inset in Fig. 5a-2 and Fig. S12). These results are verified by SEM characterization, where the concentration of the bacteria in the treated wounds is significantly lower than that in the control wounds (Fig. 5a-3 and b-3, and Fig. S13). The bacteria in the control group form biofilms, hindering wound-healing (Fig. S13c). In addition, a large epidermal and dermal area is damaged in the control group (Fig. 5b-4 and Fig. S14), causing tissue inflammation. In contrast, the skin structure of the treated group is intact (Fig. 5c-4 and Fig. S14), evidencing the potent *in vivo* anti-bacterial efficacy of Ag@PDA@Ag shells.

4. Conclusions

In conclusion, we propose a consecutive coating approach followed with a template sacrifice process to yield sandwich-structured Ag@PDA@Ag shells with enhanced antibacterial performance. Compared with previously work, in which either the interior or exterior of the particles were decorated with bioactive Ag nanoparticles [12,13,19,22,25], our sandwich-structured Ag@PDA@Ag shells exhibit an intense and lasting release of Ag ions, leading to prolonged inhibition of bacterial growth in nutritious conditions. This enhanced bioactivity is ascribed to the unique sandwich structure of the samples, in which the external Ag shells offer a rapid and intense release of Ag ions because of the direct contact to the surroundings, while the internal Ag shells provide a slow yet sustained release of Ag ions due to the obstruction of the PDA shells. Based on their superior antibacterial activity and biocompatibility with cells, we further employ these Ag@PDA@Ag shells in the *in vivo* treatment of bacterial infection. These shells are found potently against the bacterial infection caused by methicillin-resistant *Staphylococcus aureus* superbugs and enable to inhibit the biofilm formation. Our results represent a useful paradigm for the construction of antibacterial materials with augmented functional properties. With rational adaption, we believe that the designing concept of sandwich structure can be generally applied for strengthening one particular feature of the materials, catering a variety of practical extreme demands.

Acknowledgements

The authors acknowledge the National Natural Science Foundation of China (No. 51473089 and 21875189), the Natural Science Basic Research Plan in Shaanxi Province of China (No.2018JM5093 and 2015JQ5139), the Program for Science & Technology Innovation Team of Shaanxi Province (No.2018TD-030) and the Fundamental Research Funds for the Central

Universities (No.GK201702009, GK201901002) for financial support. B. P. thanks support from Marie Curie actions (CADOACCFAP, No. 796280).

Data availability

The authors confirm that there are no known conflicts of interest associated with this publication and there has been no significant financial support for this work that could have influenced its outcome. The raw and processed data required to reproduce these findings are available upon request from zwdeng@snnu.edu.cn.

Appendix A. Supplementary material

Supplementary material associated with this article can be found, in the online version, at http://dx.doi.org/

References

[1] J.W. Alexander, History of the medical use of silver, Surg. Infect. 10 (2009) 289–292.
[2] B. Peng, X. Zhang, D.G.A.L. Aarts, R.P.A. Dullens, Superparamagnetic nickel colloidal nanocrystal clusters with antibacterial activity and bacteria binding ability, Nat. Nanotechnol. 13 (2018) 478–482.
[3] Harold C. Neu, The crisis in antibiotic resistance, Science. 257 (1992) 1064–1073.
[4] T.F. Schaberle, I.M. Hack, Overcoming the current deadlock in antibiotic research, Trends Microbiol. 22 (2014) 165–167.
[5] R. Langer, D.A. Tirrell, Designing materials for biology and medicine, Nature. 428 (2004) 487–492.
[6] J.T. Seil, T.J. Webster, Antimicrobial applications of nanotechnology: methods and literature, Int. J. Nanomedicine. 7 (2012) 2767–2781.
[7] S. Chernousova, M. Epple, Silver as antibacterial agent: Ion, nanoparticle, and metal, Angew. Chemie Int. Ed. 52 (2013) 1636–1653.
[8] M. Rai, A. Yadav, A. Gade, Silver nanoparticles as a new generation of antimicrobials, Biotechnol. Adv. 27 (2009) 76–83.
[9] J.S. Kim, E. Kuk, K.N. Yu, J.-H. Kim, S.J. Park, H.J. Lee, S.H. Kim, Y.K. Park, Y.H. Park, C.-Y. Hwang, Y.-K. Kim, Y.-S. Lee, D.H. Jeong, M.-H. Cho, Antimicrobial effects of silver

nanoparticles, Nanomedicine Nanotechnology, Biol. Med. 3 (2007) 95–101.
[10] A.D. Russell, F.R.C. Path, F.R. Pharm.S., W.B. Hugo, F.R. Pharm.S., Antimicrobial Activity and Action of Silver, Prog. Med. Chem. 31 (1994) 351–370.
[11] A.P. Richter, J.S. Brown, B. Bharti, A. Wang, S. Gangwal, K. Houck, E.A.C. Hubal, V.N. Paunov, S.D. Stoyanov, O.D. Velev, An envrionmentally benign antimicrobial nanoparticle based on a silver-infused lignin core, Nat. Nanotechnol. 10 (2015) 817–823.
[12] Y. Cong, T. Xia, M. Zou, Z. Li, B. Peng, D. Guo, Z. Deng, Mussel-inspired polydopamine coating as a versatile platform for synthesizing polystyrene/Ag nanocomposite particles with enhanced antibacterial activities, J. Mater. Chem. B. 2 (2014) 3450–3461.
[13] M. Liong, B. France, K.A. Bradley, J.I. Zink, Antimicrobial activity of silver nanocrystals encapsulated in mesoporous silica nanoparticles, Adv. Mater. 21 (2009) 1684–1689.
[14] Z. Deng, M. Chen, A. Gu, L. Wu, A facile method to fabricate ZnO hollow spheres and their photocatalytic property, J. Phys. Chem. B. 112 (2008) 16–22.
[15] Z. Deng, M. Chen, L. Wu, Novel Method to Fabricate SiO2/Ag Composite Spheres and Their Catalytic , Surface-Enhanced Raman Scattering Properties, J. Phys. Chem. C. 111 (2007) 11692–11698.
[16] Y. Xiong, I. Washio, J. Chen, H. Cai, Z.-Y. Li, Y. Xia, Poly(vinyl pyrrolidone): a dual functional reductant and stabilizer for the facile synthesis of noble metal nanoplates in aqueous solutions., Langmuir. 22 (2006) 8563–70.
[17] A. Imhof, Preparation and Characterization of Titania-Coated Polystyrene Spheres and Hollow Titania Shells, Langmuir. 17 (2001) 3579–3585.
[18] C. Graf, D.L.J. Vossen, A. Imhof, A. van Blaaderen, A General Method To Coat Colloidal Particles with Silica, Langmuir. 19 (2003) 6693–6700.
[19] K. Zhao, J. Zhao, C. Wu, S. Zhang, Z. Deng, X. Hu, M. Chen, B. Peng, Fabrication of silver-decorated sulfonated polystyrene microspheres for surface-enhanced Raman scattering and antibacterial applications, RSC Adv. 5 (2015) 69543–69554.
[20] H. Lee, S.M. Dellatore, W.M. Miller, P.B. Messersmith, Mussel-Inspired Surface Chemistry for Multifunctional Coatings, Science. 318 (2007) 426–430.
[21] H. Lee, Y. Lee, A.R. Statz, J. Rho, T.G. Park, P.B. Messersmith, Substrate-independent layer-by-layer assembly by using mussel-adhesive- inspired polymers, Adv. Mater. 20 (2008) 1619–1623.
[22] C. Wu, G. Zhang, T. Xia, Z. Li, K. Zhao, Z. Deng, D. Guo, B. Peng, Bioinspired synthesis of polydopamine/Ag nanocomposite particles with antibacterial activities, Mater. Sci. Eng. C. 55 (2015) 155–165.
[23] C. Wu, Z. Deng, B. Shang, O. Ikkala, B. Peng, A versatile colloidal Janus platform: Surface asymmetry control, functionalization, and applications, Chem. Commun. 54 (2018) 12726–12729.
[24] Y. Wang, B. Shang, M. Liu, F. Shi, B. Peng, Z. Deng, Hollow polydopamine colloidal composite particles: Structure tuning, functionalization and applications, J. Colloid Interface Sci. 513 (2018) 43–52.
[25] Z. Deng, B. Shang, B. Peng, Polydopamine Based Colloidal Materials: Synthesis and Applications, Chem. Rec. 18 (2018) 410–432.
[26] Y. Liu, K. Ai, L. Lu, Polydopamine and its derivative materials: Synthesis and promising applications in energy, environmental, and biomedical fields, Chem. Rev. 114 (2014) 5057–5115.
[27] Y. Wang, A.G. El-Deen, P. Li, B.H.L. Oh, Z. Guo, M.M. Khin, Y.S. Vikhe, J. Wang, R.G. Hu, R.M. Boom, K.A. Kline, D.L. Becker, H. Duan, M.B. Chan-Park, High-Performance Capacitive Deionization Disinfection of Water with Graphene Oxide-graft-Quaternized Chitosan Nanohybrid Electrode Coating, ACS Nano. 9 (2015) 10142–10157.
[28] Y. Su, Z. Zhi, Q. Gao, M. Xie, M. Yu, B. Lei, P. Li, P.X. Ma, Autoclaving-Derived Surface Coating with In Vitro and In Vivo Antimicrobial and Antibiofilm Efficacies, Adv. Healthc. Mater. 6 (2017) 1601173.
[29] A.E. Krausz, B.L. Adler, V. Cabral, M. Navati, J. Doerner, R.A. Charafeddine, D. Chandra, H. Liang, L. Gunther, A. Clendaniel, S. Harper, J.M. Friedman, J.D. Nosanchuk, A.J.

Friedman, Curcumin-encapsulated nanoparticles as innovative antimicrobial and wound healing agent, Nanomedicine Nanotechnology, Biol. Med. 11 (2015) 195–206.
[30] P.G. Bowler, B.I. Duerden, D.G. Armstrong, Wound Microbiology and Associated Approaches to Wound, Clin. Microbiol. Rev. 14 (2001) 244–269.
[31] P. Li, Y.F. Poon, W. Li, H.Y. Zhu, S.H. Yeap, Y. Cao, X. Qi, C. Zhou, M. Lamrani, R.W. Beuerman, E.T. Kang, Y. Mu, C.M. Li, M.W. Chang, S.S. Jan Leong, M.B. Chan-Park, A polycationic antimicrobial and biocompatible hydrogel with microbe membrane suctioning ability, Nat. Mater. 10 (2011) 149–156.
[32] I. Washio, Y. Xiong, Y. Yin, Y. Xia, Reduction by the End Groups of Poly(vinyl pyrrolidone): A New and Versatile Route to the Kinetically Controlled Synthesis of Ag Triangular Nanoplates, Adv. Mater. 18 (2006) 1745–1749.
[33] B. Shang, Y. Wang, B. Peng, Z. Deng, Bioinspired polydopamine particles-assisted construction of superhydrophobic surfaces for oil/water separation, J. Colloid Interface Sci. 482 (2016) 240–251.
[34] T. Xia, M. Kovochich, M. Liong, J.I. Zink, A.E. Nel, Cationic Polystyrene Nanosphere Toxicity Depends on Cell-Specific Endocytic and Mitochondiral Injury Pathways, ACS Nano. 2 (2008) 85–96.
[35] H.W. Chiu, T. Xia, Y.H. Lee, C.W. Chen, J.C. Tsai, Y.J. Wang, Cationic polystyrene nanospheres induce autophagic cell death through the induction of endoplasmic reticulum stress, Nanoscale. 7 (2015) 736–746.
[36] X.W.D. Lou, L.A. Archer, Z. Yang, Hollow Micro-/Nanostructures: Synthesis and Applications, Adv. Mater. 20 (2008) 3987–4019.
[37] J. Hu, M. Chen, X. Fang, L. Wu, Fabrication and application of inorganic hollow spheres, Chem. Soc. Rev. 40 (2011) 5472–5491.
[38] P. V. AshaRani, G.L.K. Mun, M.P. Hande, S. Valiyaveettil, Cytotoxicity and Genotoxicity of Silver Nanomaterials in Human Cells, ACS Nano. 3 (2009) 279–290.
[39] L. Zhao, H. Wang, K. Huo, L. Cui, W. Zhang, H. Ni, Y. Zhang, Z. Wu, P.K. Chu, Antibacterial Nano-Structured Titania Coating Incorporated with Silver Nanoparticles, Biomaterials. 32 (2011) 5706–5716.
[40] J.R. Morones, J.L. Elechiguerra, A. Camacho, K. Holt, J.B. Kouri, J.T. Ramírez, M.J. Yacaman, The bactericidal Effect of Silver Nanoparticles, Nanotechnology. 16 (2005) 2346–2353.

Figure captions

Fig. 1. Synthesis and characterization of sandwich-structured Ag@polydopamine@Ag shells. a) Synthesis of Ag@PDA@Ag shells, including: 1-PVP-assisted Ag nanoparticle decoration, yielding sulfonated polystyrene@Ag nanoparticle core-shell particles, SPS@Ag; 2-PDA encapsulation, SPS@Ag@PDA; 3-*in situ* reduction of $[Ag(NH_3)_2]^+$ ions with PDA, SPS@Ag@PDA@Ag; 4-SPS core removal, Ag@PDA@Ag. Transmission electron microscopy

(TEM) observations b-f) and X-ray photoelectron spectroscopy characterizations g) of samples from each step: b) SPS, c) SPS@Ag, d) SPS@Ag@PDA, e) SPS@Ag@PDA@Ag, and f) Ag@PDA@Ag. h) Dark field TEM and energy-dispersive X-ray spectroscopy-based elemental mapping analysis of Ag@PDA@Ag shells. Scale bars are 2 μm.

Fig. 2. Selective size control of inner and outer Ag nanoparticles. TEM observations of Ag@PDA shells synthesized with different amounts of Ag precursors from a) Ag@PDA-i, 0.29 to b) Ag@PDA-ii, 0.58, c) Ag@PDA-iii, 0.88, and d) Ag@PDA-iv, 1.17 mM; e) Size distributions of Ag nanoparticles in samples a)-d); TEM and SEM observations of size tuning of the outer Ag nanoparticles in Ag@PDA@Ag by altering the amount of Ag precursors from f) Ag@PDA@Ag-i, 0.6 to g) Ag@PDA@Ag-ii, 1.20, and h) Ag@PDA@Ag-iii, 2.40 mM; Size distributions of outer Ag nanoparticles in samples f)-h). The amount of Ag precursor used to construct the interior Ag shells in f)-h) is 1.17 mM. For more details on the synthetic ingredients and sizes see Table S2. Scale bars are 1 μm.

Fig. 3. Antibacterial evaluation and Ag+ ion release analysis of Ag-PDA nanocomposite shells. Photographs of the incubation of shells (100 μg/mL) with a) Gram-negative *Escherichia coli* ATCC 25922 and b) Gram-positive *Staphylococcus aureus* ATCC 29213 bacteria on Lysogeny broth-agar plates; c) Bacterial growth in Mueller-Hinton broths with shells (100 μg/mL) as a function of incubation time for c) *E. coli* and d) *S. aureus*.; e) Monitoring the concentration of Ag^+ ions released from shells with time; f) Ag^+ ion release rate as a function of time. Note, the concentrates of the shells are fixed at 100 μg/mL throughout all experiments. The details of the shells are summarized in Table S2.

Fig. 4. *In vitro* hemolysis assay a) and cytotoxicity evaluation b) of Ag@PDA@Ag shells with rat erythrocyte cells and C2C12 cells, respectively.

Fig. 5. *In vivo* anti-bacterial infection experiments. Photographs of rat's wounds created by incising the skin taken on day 0, a-1) and b-1), and day 4 after infection by methicillin-resistant *S. aureus* superbugs a-2) without and b-2) with treatment with Ag@PDA@Ag-iii shells (control and treated batch, respectively). The insets are the incubated viable bacteria on LB-agar plates; Representative SEM characterization of skin tissue from the control a-3) and the treated wound b-3); Representative histological analysis of the tissue adjacent to the control and treated batch. Note that the red arrows point out areas of inflammation (neutrophil cells).

Figures

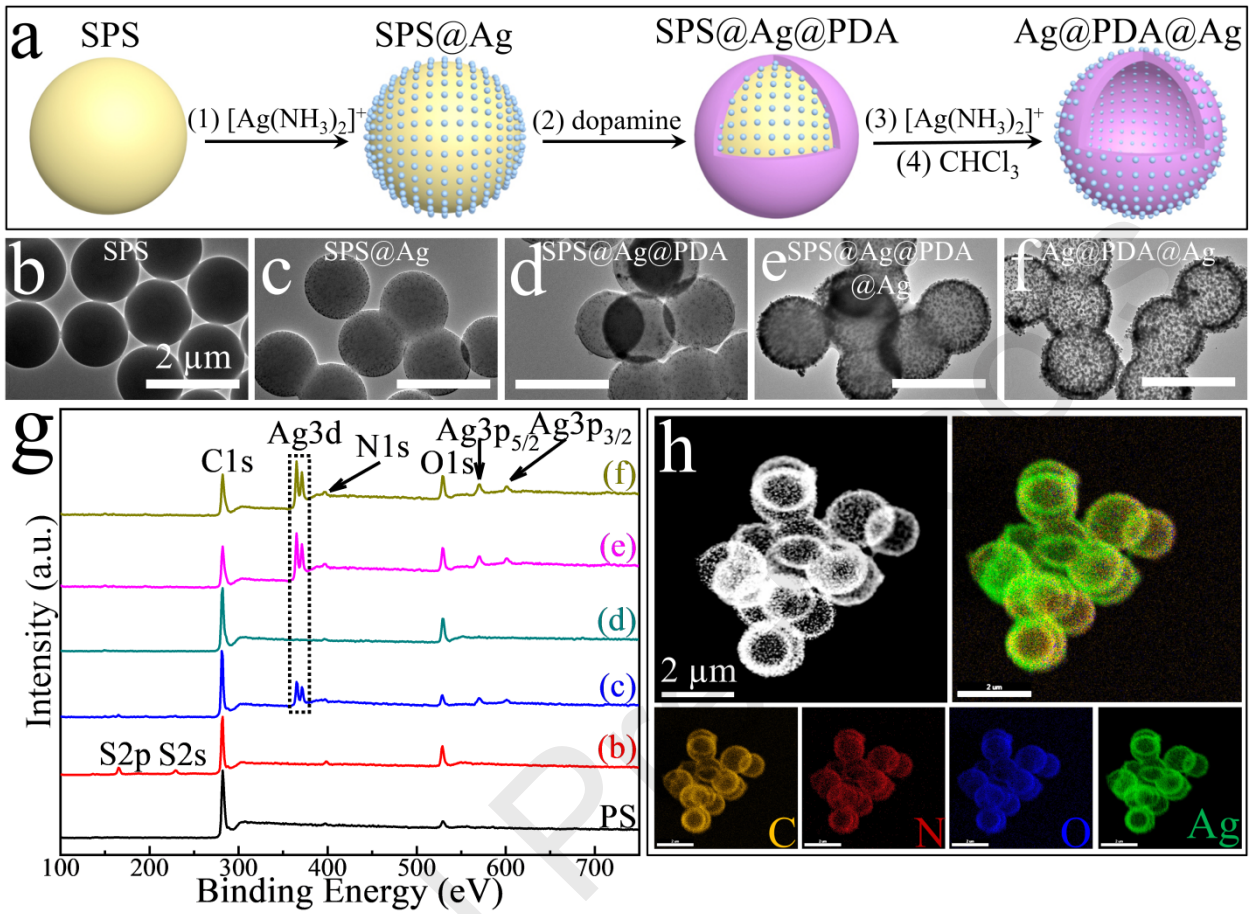

Fig. 1. Synthesis and characterization of sandwich-structured Ag@polydopamine@Ag shells. a) Synthesis of Ag@PDA@Ag shells, including: 1-PVP-assisted Ag nanoparticle decoration, yielding sulfonated polystyrene@Ag nanoparticle core-shell particles, SPS@Ag; 2-PDA encapsulation, SPS@Ag@PDA; 3-*in situ* reduction of $[Ag(NH_3)_2]^+$ ions with PDA, SPS@Ag@PDA@Ag; 4-SPS core removal, Ag@PDA@Ag. Transmission electron microscopy (TEM) observations b-f) and X-ray photoelectron spectroscopy characterizations g) of samples from each step: b) SPS, c) SPS@Ag, d) SPS@Ag@PDA, e) SPS@Ag@PDA@Ag, and f) Ag@PDA@Ag. h) Dark field TEM and energy-dispersive X-ray spectroscopy-based elemental mapping analysis of Ag@PDA@Ag shells. Scale bars are 2 μm.

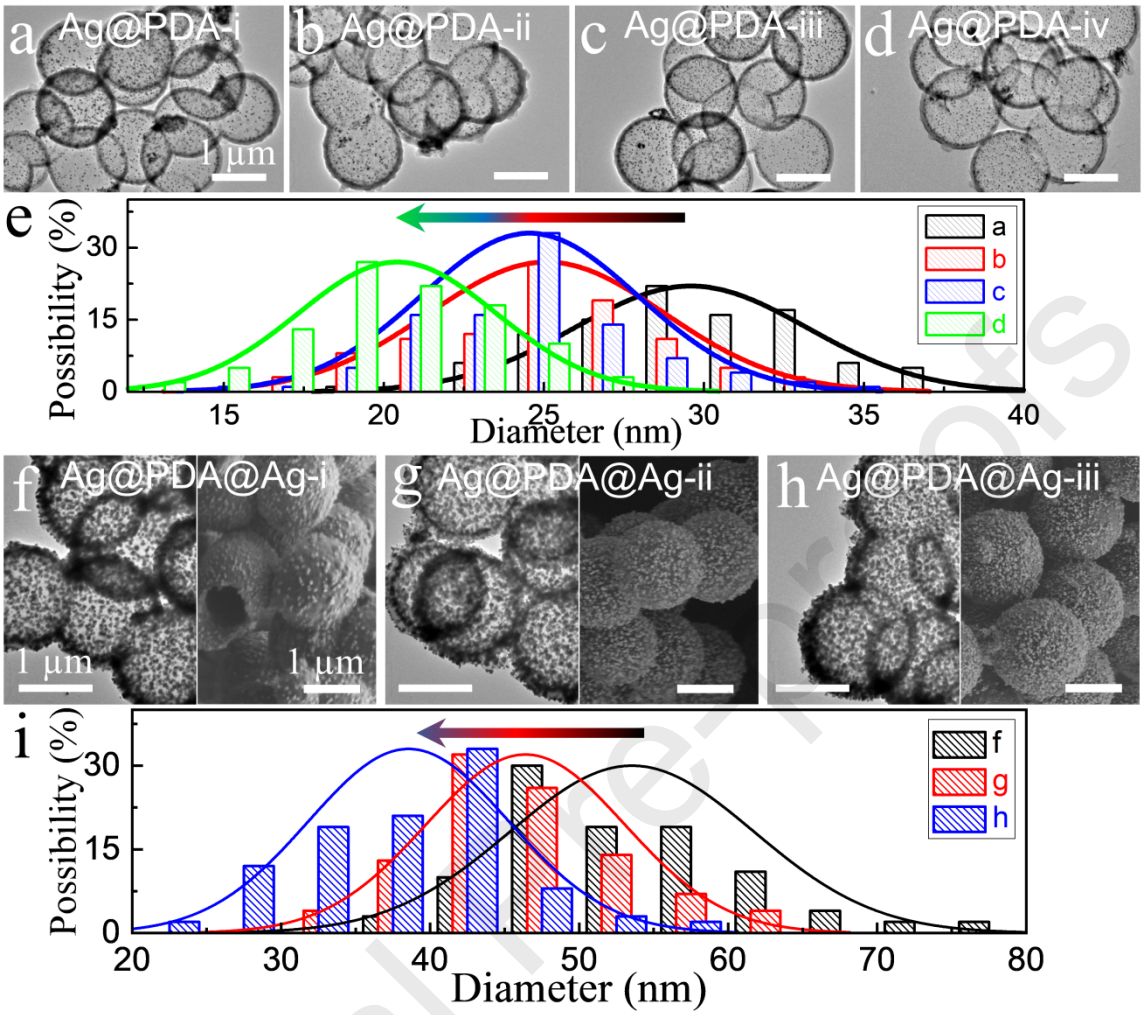

Fig. 2. Selective size control of inner and outer Ag nanoparticles. TEM observations of Ag@PDA shells synthesized with different amounts of Ag precursors from a) Ag@PDA-i, 0.29 to b) Ag@PDA-ii, 0.58, c) Ag@PDA-iii, 0.88, and d) Ag@PDA-iv, 1.17 mM; e) Size distributions of Ag nanoparticles in samples a)-d); TEM and SEM observations of size tuning of the outer Ag nanoparticles in Ag@PDA@Ag by altering the amount of Ag precursors from f) Ag@PDA@Ag-i, 0.6 to g) Ag@PDA@Ag-ii, 1.20, and h) Ag@PDA@Ag-iii, 2.40 mM; Size distributions of outer Ag nanoparticles in samples f)-h). The amount of Ag precursor used to construct the interior Ag shells in f)-h) is 1.17 mM. For more details on the synthetic ingredients and sizes see Table S2. Scale bars are 1 μm.

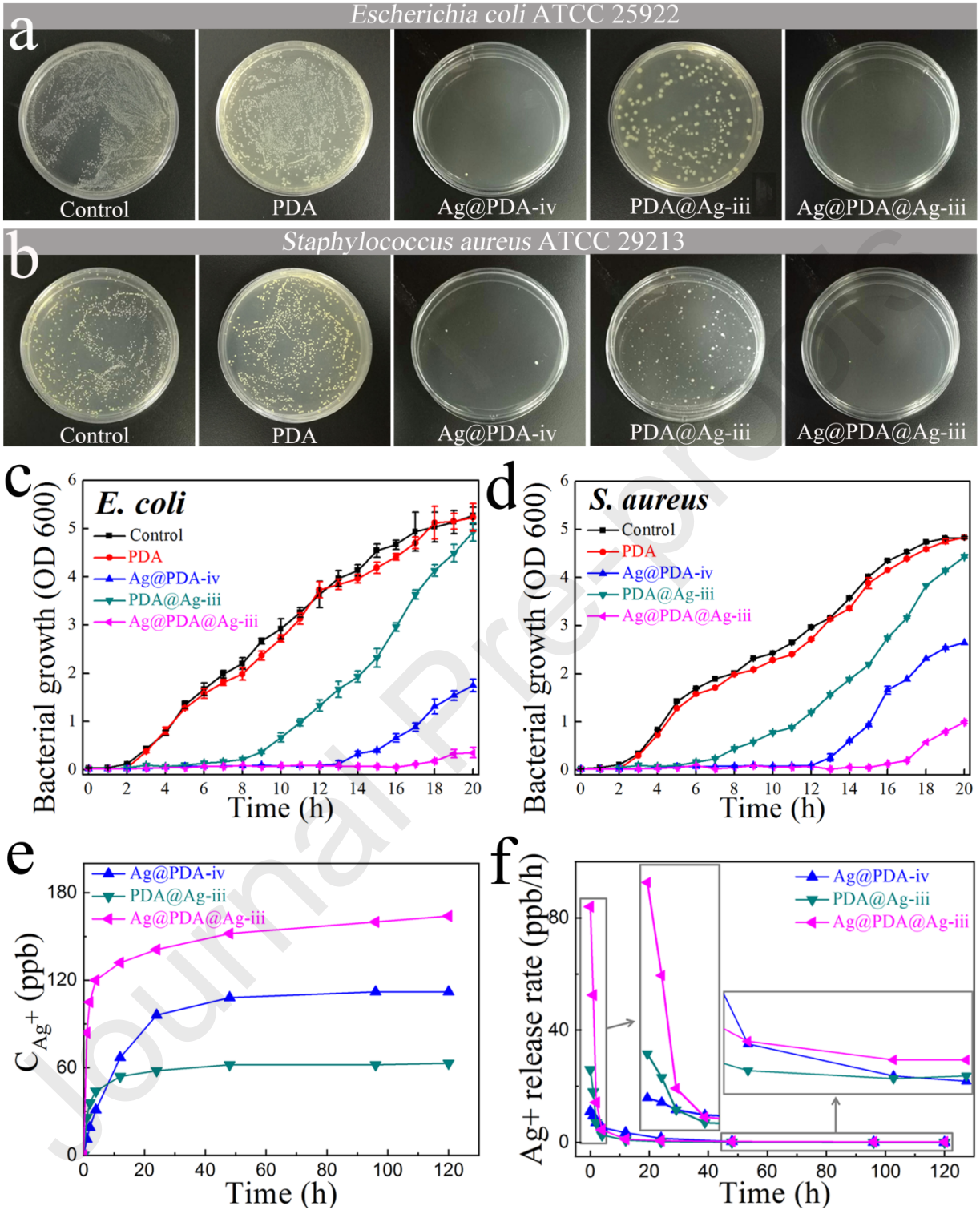

Fig. 3. Antibacterial evaluation and Ag+ ion release analysis of Ag-PDA nanocomposite shells. Photographs of the incubation of shells (100 μg/mL) with a) Gram-negative *Escherichia coli* ATCC 25922 and b) Gram-positive *Staphylococcus aureus* ATCC 29213 bacteria on Lysogeny

broth-agar plates; c) Bacterial growth in Mueller-Hinton broths with shells (100 μg/mL) as a function of incubation time for c) *E. coli* and d) *S. aureus*.; e) Monitoring the concentration of Ag^+ ions released from shells with time; f) Ag^+ ion release rate as a function of time. Note, the concentrates of the shells are fixed at 100 μg/mL throughout all experiments. The details of the shells are summarized in Table S2. Data are means of three repeats, and error bars indicate standard deviations.

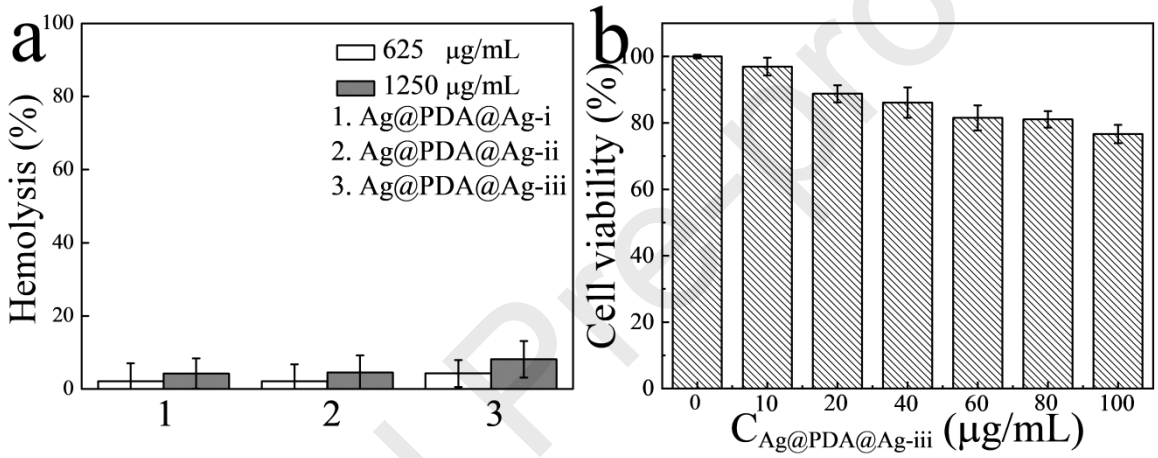

Fig. 4. *In vitro* hemolysis assay a) and cytotoxicity evaluation b) of Ag@PDA@Ag shells with rat erythrocyte cells and C2C12 cells, respectively. Data are means of three repeats, and error bars indicate standard deviations.

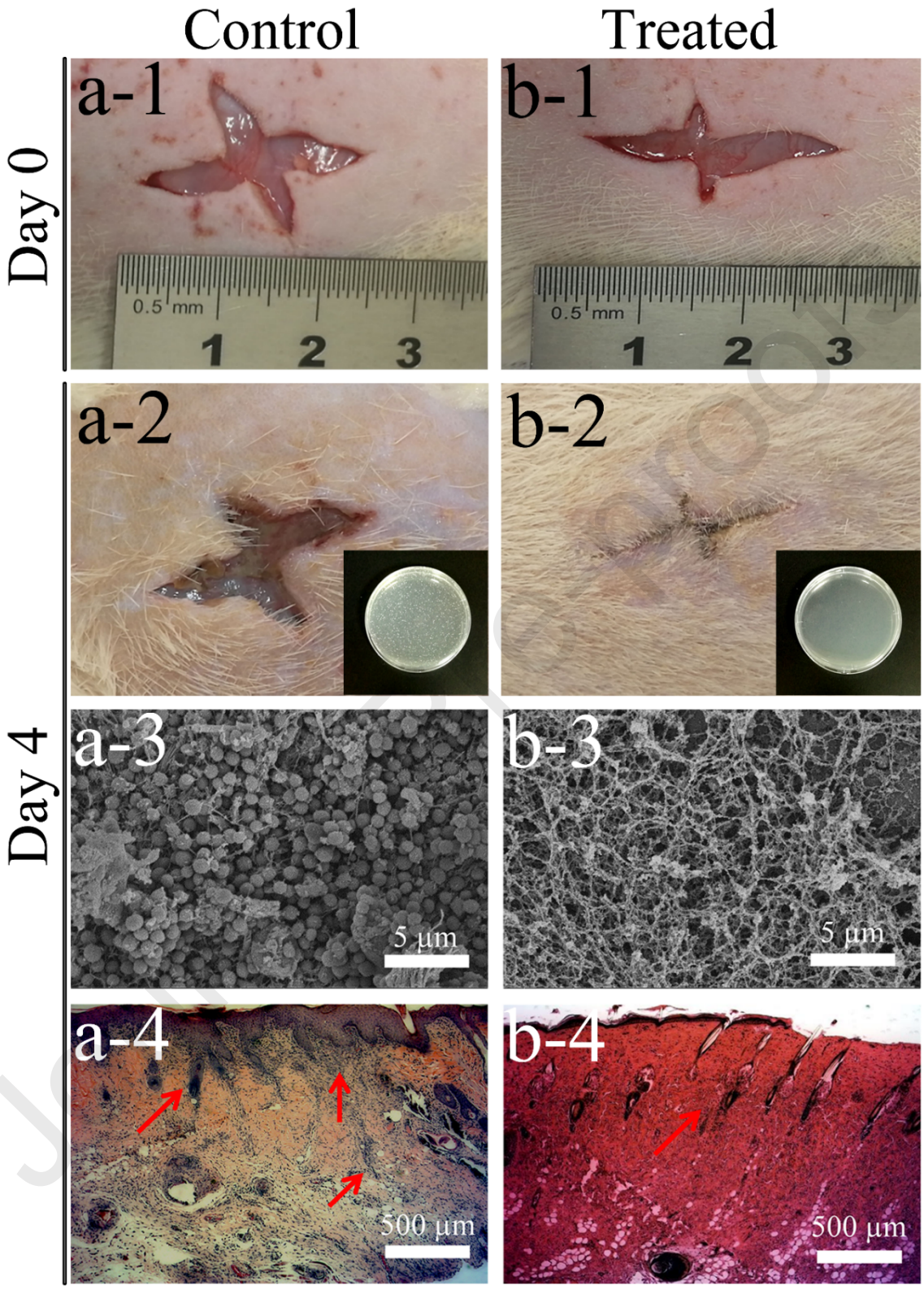

Fig. 5. *In vivo* anti-bacterial infection experiments. Photographs of rat's wounds created by incising the skin taken on day 0, a-1) and b-1), and day 4 after infection by methicillin-resistant *S.*

aureus superbugs a-2) without and b-2) with treatment with Ag@PDA@Ag-iii shells (control and treated batch, respectively). The insets are the incubated viable bacteria on LB-agar plates; Representative SEM characterization of skin tissue from the control a-3) and the treated wound b-3); Representative histological analysis of the tissue adjacent to the control and treated batch. Note that the red arrows point out areas of inflammation (neutrophil cells).

Graphical abstract